



Research Paper

Nanodiamonds in sp^2/sp^3 configuration for radical to nonradical oxidation: Core-shell layer dependence



Xiaoguang Duan^a, Zhimin Ao^{b,*}, Huayang Zhang^a, Martin Saunders^c, Hongqi Sun^{d,*},
Zongping Shao^{a,e}, Shaobin Wang^{a,*}

^a Department of Chemical Engineering, Curtin University, GPO Box U1987, WA 6845, Australia

^b Institute of Environmental Health and Pollution Control, School of Environmental Science and Engineering, Guangdong University of Technology, Guangzhou, 510006, China

^c Centre for Microscopy, Characterization and Analysis, The University of Western Australia, Crawley, WA, 6009, Australia

^d School of Engineering, Edith Cowan University, Joondalup, WA 6027, Australia

^e College of Chemical Engineering, Nanjing Tech University, Nanjing 210009, China

ARTICLE INFO

Keywords:

Nanodiamond
Carbocatalysis
Peroxymonosulfate
Nonradical
DFT

ABSTRACT

Nanocarbons in molecular configurations of sp^2/sp^3 present versatile structural and electronic properties, exhibiting a complexity in the structure-activity chemistry. In this work, we employed detonation nanodiamonds constructed as a characteristic core/shell structure in the sp^2/sp^3 configuration to demonstrate the intrinsic correlation between the structure and catalysis. Annealed detonation nanodiamonds were found to show a superb activity for catalytic peroxymonosulfate activation and organic oxidation. A synergistic effect of charge transport was discovered at the interface to construct an electron-enriched carbon surface that further promoted the catalytic activity evidenced by the density functional theory (DFT) calculations. More importantly, both experimental results and theoretical predictions revealed that the catalytic oxidation via peroxymonosulfate (PMS) activation was intimately dependent on the proportion of graphitic carbon layer in the sp^2/sp^3 configurations. The increase of graphitic layers on nanodiamonds would alter the PMS activation from a radical-based reaction to a nonradical pathway for catalytic oxidation. The novel catalytic properties of tunable oxidative potentials from carbocatalysis may simulate fascinating prospects for environmental catalysis and organic synthesis.

1. Introduction

The state-of-the-art carbocatalysis has appealed great passions in the scientific community of electrochemistry and heterogeneous reactions owing to the fascinating physicochemical properties and metal-free nature of nanocarbon materials [1,2]. The intrinsic reactivity of graphitic carbon allotropes (graphene, carbon nanotubes etc.) has been illustrated to be intimately associated with the distorted carbon domains (activated by alien-atom doping) and the versatile defective sites as well as functional groups that exhibit unique electronic/spin cultures [3–6]. Manipulation of both the structure and functionality would offer a tool for tailoring the opening bandgap, enhancing the light-harvest capability, and promoting the charge transport/separation. To this end, nanocarbon hybridization using two or more compounds has been commonly proposed to achieve novel properties, attributing to the hetero-interacted interfaces and electron tunnelling effects [7–9]. However, for a mechanistic study, the active sites of the hybrids in

carbocatalysis are far more complicated and difficult to be elucidated.

Nanodiamonds (NDs) produced from a detonation method are comprised of a highly sp^3 -hybridized nanocrystal (5 ± 2 nm) in an irregular morphology with a high surface/volume ratio. NDs are normally terminated with hydrogen and oxygen atoms and partially covered by amorphous soot. Thermal annealing is able to eliminate the surface contaminants and partially decompose the outer sphere of the nanodiamonds to form a graphitic fullerene shell, hereby transforming the bulk nanocrystal into a uniform and self-assembled sp^2/sp^3 hybrid structure [10,11]. The graphitization of nanodiamonds involves multi-steps. At a low temperature range (300–800 °C), it would lead to de-attachment of moisture and oxygen functionalities (carboxyl, hydroxyl, and ketonic groups), and decomposition of surface soot and amorphous carbon [12,13]. When further annealing nanocrystals at above 900 °C, the carbon atoms at the terminal grain boundaries of sp^3 -hybridized diamond crystals would be rearranged into a π -conjugated framework, which will subsequently be constructed into a graphitic shell which

* Corresponding authors.

E-mail addresses: zhimin.ao@gdut.edu.cn (Z. Ao), h.sun@ecu.edu.au (H. Sun), shaobin.wang@curtin.edu.au (S. Wang).

<http://dx.doi.org/10.1016/j.apcatb.2017.10.007>

Received 10 July 2017; Received in revised form 3 October 2017; Accepted 6 October 2017

Available online 06 October 2017

0926-3373/ © 2017 Elsevier B.V. All rights reserved.

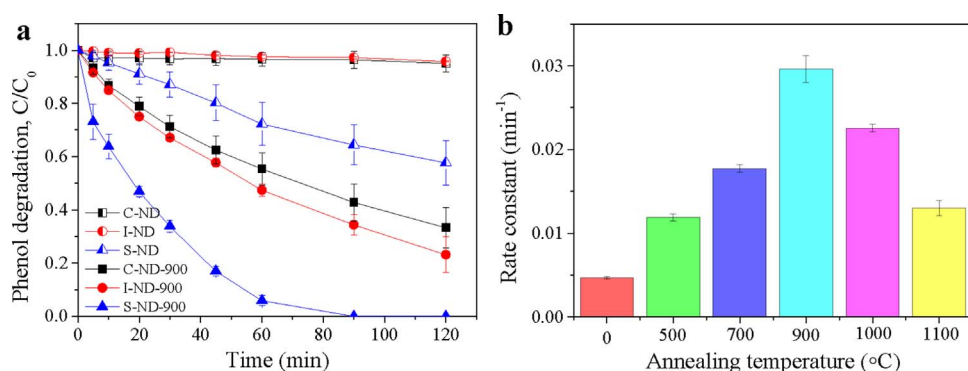


Fig. 1. (a) Carbocatalysis on pristine and graphitized nanodiamonds from different sources, and (b) effect of annealing temperature on the catalytic performance of S-ND.

covers the sp^3 diamond structure [14,15]. The removal of oxygen functionalities on outer sphere of diamond can also bring in structural defects and dangling bonds for further promoting the collapse and transition of sp^3 carbon to sp^2 network [16]. Therefore, the structure of nanodiamonds can be easily regulated by thermal annealing at high temperatures under inert/oxidative ambience to facilitate a mechanistic study that cannot be done on carbon hybrids.

Benefited from a characteristic core/shell architecture, the partially graphitized nanodiamonds may present a novel catalytic behavior of the graphene-based materials meanwhile embracing new properties from the diamond part via a delicate sp^2/sp^3 control. The graphite/diamond structure has demonstrated a better activity than other carbon materials in oxidative dehydrogenation (ODH) reactions [14,17]. However, such a synergistic effect was barely investigated in the aqueous-phase reactions, and the impacts of the shell thickness on the electronic/geometric variations, i.e. diamond-based catalysis mechanism, have not been elucidated yet. Here we reported a case study of catalytic oxidation from peroxymonosulfate (PMS) activation on controlled graphitized nanodiamonds. This study helps reveal the relevance between the structural transformation and catalytic activity in carbocatalysis. We discovered that the new creation of graphitic carbon layer on nanodiamonds would greatly promote the PMS activation, meanwhile the rational rearrangement of sp^2/sp^3 configurations induces different reaction pathways towards catalytic oxidation.

2. Experimental

2.1. Chemicals and catalyst synthesis

Three nanodiamonds, such as I-ND (Ray Techniques Ltd., Israel), C-ND (XFnano Materials Tech Co. Ltd., China), and S-ND (< 10 nm, Sigma-Aldrich, Australia), were received and purified by thoroughly acid washing to remove the potential metal residues. Then, the pristine nanodiamonds were placed in a tubular quartz reactor and treated by thermal annealing under nitrogen at 5 °C/min and held at 500–1100 °C (donated as ND-X, X = 500–1100) for 1 h. The derived samples were cooled down naturally, washed with ethanol (70 wt%) and ultrapure water, and dried at 60 °C in an oven.

2.2. Characterizations of carbon materials

The structure of nanodiamonds was revealed by high-resolution transmission electron microscopy (HRTEM) images acquired on a Titan G2 80–200 TEM at 80 kV. The electron energy loss spectra (EELS) at high and low energy regions were analyzed on the same TEM at 120 kV. X-ray photoelectron spectroscopy (XPS) was employed to estimate the elemental composition of nanodiamond surface under ultrahigh vacuum conditions ($< 1 \times 10^{-9}$ mBar) on a Kratos AXIS Ultra DLD system. The surface property and porous structure of nanodiamonds were measured at liquid nitrogen temperature (−196 °C) on a TriStar instrument and calculated by the Brunauer-Emmett-Teller (BET) and

Barret-Joyner-Halenda (BJH) equations. The crystalline information of nanodiamonds were analyzed by X-ray diffraction (XRD) with a Cu K α X-ray gun ($\lambda = 1.5418$ Å). Electron paramagnetic resonance (EPR) was performed to analyze the spin numbers of structural defects in nanodiamonds. In a typical analysis, the nanodiamond power was placed in the center of the EPR instrument. The EPR parameters were recorded as [Sweep width] = 200 G, [Sweep time] = 30 min, [g-factor] = 2.003, [Attenuation] = 12.7 dB, [Center field] = 3517.75 G, and [Power] = 9.98 mW.

2.3. Catalytic performance evaluation

The experiments were conducted with the dosages of the chemicals and catalysts as carbocatalysts (0.1 g/L), target organics (20 mg/L phenol), and the oxidant (PMS, 2 g/L). The reactor system was kept stirring at 400 rpm at 25 °C to form a homogeneous suspension. At set time intervals, the solution mixture was filtered via a 0.45 μ m membrane to remove the solids and mixed with methanol to react with the remaining free radicals in the filtrate. Phenol concentrations were detected on a Thermal-Fisher high-performance liquid chromatography (HPLC) with an OA column at 270 nm.

3. Results and discussion

3.1. Catalyst characterization and performance

Firstly, the catalytic activity of pristine and annealed nanodiamonds (NDs) from different sources were screened. As indicated in Fig. 1a, the pristine nanodiamonds e.g. C-ND (XFnano Materials Tech Co. Ltd, China) and I-ND (Ray Techniques Ltd., Israel) can hardly decompose PMS to generate reactive species for phenol decomposition. Only around 42.3% phenol removal was achieved on S-ND (Sigma-Aldrich, Australia). However, it was proved that the catalytic performance of the pristine nanodiamonds can be significantly improved by thermal annealing (900 °C, Fig. S1). For example, C-ND-900 and I-ND-900 attained 66.7% and 76.9% organic removals in 120 min, respectively, and S-ND-900 yielded complete phenol degradation in 90 min with PMS. Fig. S2 and Table S1 show that the specific surface areas (SSAs) of the nanodiamonds were slightly increased after the high-temperature treatment because of the thermal expansion of highly stacked nanoparticles. The high surface energy of nanoscaled crystals gives rise to the aggression of nanodiamonds. Interestingly, S-ND-900 possesses the lowest surface area (365 m²/g vs 394 m²/g of C-ND-900 and 375 m²/g of I-ND-900) yet demonstrates the highest activity, suggesting that the surface area is not the key factor dominating the catalytic behavior. Moreover, XRD patterns (Fig. S3) illustrate that the S-ND-900 exhibited the lowest crystalline intensity among the three annealed nanodiamonds, which might facilitate the decomposition of the outer shell of the diamond (111) terminating planes and transformation into a graphitic (001) shell [18,19]. Meanwhile, the texture of the denotating nanodiamonds from different sources may also influence the annealing processes as well as

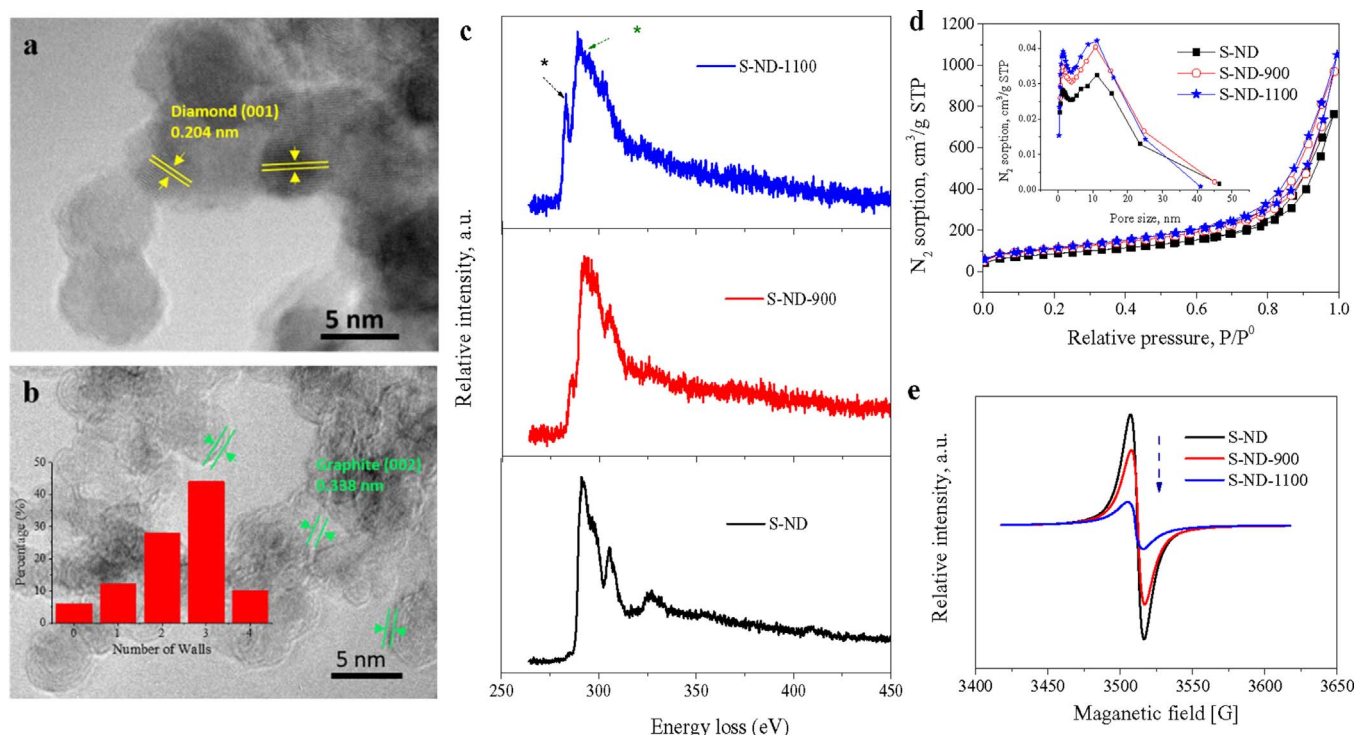


Fig. 2. TEM images of (a) S-ND and (b) S-ND-1100. (c) Electron energy loss spectra, (d) Nitrogen sorption profiles and pore size distributions (inset), and (e) Electron resonance of various nanodiamonds.

the catalytic activity of the derived products. The impact of annealing temperature (500–1100 °C) on peroxymonosulfate activation and phenol oxidation was further investigated under inert ambience. It was discovered that phenol oxidation efficiency was remarkably promoted after the thermal treatment (Fig. 1b), due to the optimization of surface oxygen functionalities and reconstruction of carbon configuration [20]. Interestingly, the reaction rate constants soared from 0.0047 min⁻¹ on pristine S-ND to 0.030 min⁻¹ on S-ND-900. Then the rate declined gradually at higher temperatures with 0.023 and 0.013 min⁻¹ for S-ND-1000 and S-ND-1100, respectively. Moreover, we evaluated the metal residues of the S-NDs by strong acid (nitrohydrochloric acid) digestion. It was found that only very trace metal element (Fe) was detected in S-ND, suggesting that it is the carbocatalysis that drives PMS activation for graphitized nanodiamonds [21]. Nonetheless, the nitrogen impurities inherited from the detonation synthesis were discovered for all the nanodiamonds (Table S2), and the N impurities buried in the core exhibited an insignificant influence on the catalytic performances of the graphitized nanodiamond (Fig. 1).

The HRTEM images in Fig. 2a evidence the diamond crystal structure with a lattice spacing distance of 2.04 Å, which is in consistence with the XRD patterns with the (001) diamond facet locating at 42.5° (2θ) in Fig. S3. S-ND-500 and S-ND-700 (Fig. S3) presented a similar fingerprint. It can be found that only the bulk diamond structure can be discovered for S-ND, S-ND-500, and S-ND-700. However, a shell of graphite layer emerged for S-ND-900 and 1–2 layers occurred for S-ND-1000 (Fig. S5). When the annealing temperature climbed up to 1100 °C, the layer number of the onion-like shell increased to 2 ~ 4 shells on S-ND-1100 with a smaller diamond core of 2 ~ 3 nm as shown in Fig. 2b. However, the particle size of the multilayer encapsulated nanodiamond (S-ND-1100) slightly increased to 6–7 nm due to the expended shells, which can be further reflected by the increased SSA of 416 m²/g compared with S-ND-X (X = 500–1000) of 350–370 m²/g in Table S2.

The graphitization degree at the outer sphere of the nanodiamonds was identified by the electron energy loss spectroscopy (EELS) as depicted in Fig. 2c. Within the high-energy region, the dominant peak locating at 290.0 eV can be assigned to the typical electron transition

from 1 s core level to σ* orbits excited from the sp³-hybridized carbon of diamond crystal, whereas the shoulder peak sitting at around 283.7 eV can be stemmed from the 1 s core level to π* band (p-orbits) transitions for the sp²-hybridized graphite/graphene [14,22]. Pristine S-ND only presents a prominent peak assigned to diamond, while a weak graphite intensity is emerged on S-ND-900 implying the occurrence of graphitic layer. The 1 s → π* intensity becomes more predominant on S-ND-1100, which reveals the formation of multi-fullerene shells. Fig. S6 presents the corresponding low-loss EELS spectra of the nanodiamonds. Similarly, the S-ND presents a main peak with the plasmon energy of 35 eV associated with the bulk diamond, and the appearance of the ridge at 20 eV for S-ND-900 and S-ND-1100 could be attributed to the graphitic carbon [23]. The increment of peak intensity of graphite at higher temperatures manifested a higher graphitic degree, which is in good consistence with the high energy EELS spectra. The nitrogen sorption profiles in Fig. 2d reveal that the surface and pore volume were only slightly increased at higher temperatures, and the pore size distribution still fell in the region of micro- and meso-pores that are derived from the carbon surface and aggression of secondary diamond nano-particles.

The electron paramagnetic resonance (EPR) is an informative and nondestructive tool to detect the unpaired electrons and spins of defective sites, carbon dangling bonds, and impurities in diamond crystals [24,25]. The EPR spectra (Fig. 2e) clearly show that the EPR signal intensity (Landé factor g = 2.003) decreased dramatically after the thermal treatment, and S-ND-1100 exhibited the lowest level of paramagnetic centers. This is due to the fact that the carbon atoms in structural defects and dangling bonds at the diamond outer surface were decomposed and re-constructed into the graphitic shell during the annealing process, meanwhile leaving a smaller diamond core with fewer number of defects and dangling bonds at the grain boundaries. The EPR well illustrates the process of thermal transition from a bulk diamond to a core/shell hybrid that has already been witnessed by HRTEM and EELS above. Additionally, other advanced techniques such as Raman spectroscopy and extended X-ray absorption fine structure (EXAFS) are also powerful and nondestructive tools to analyze the

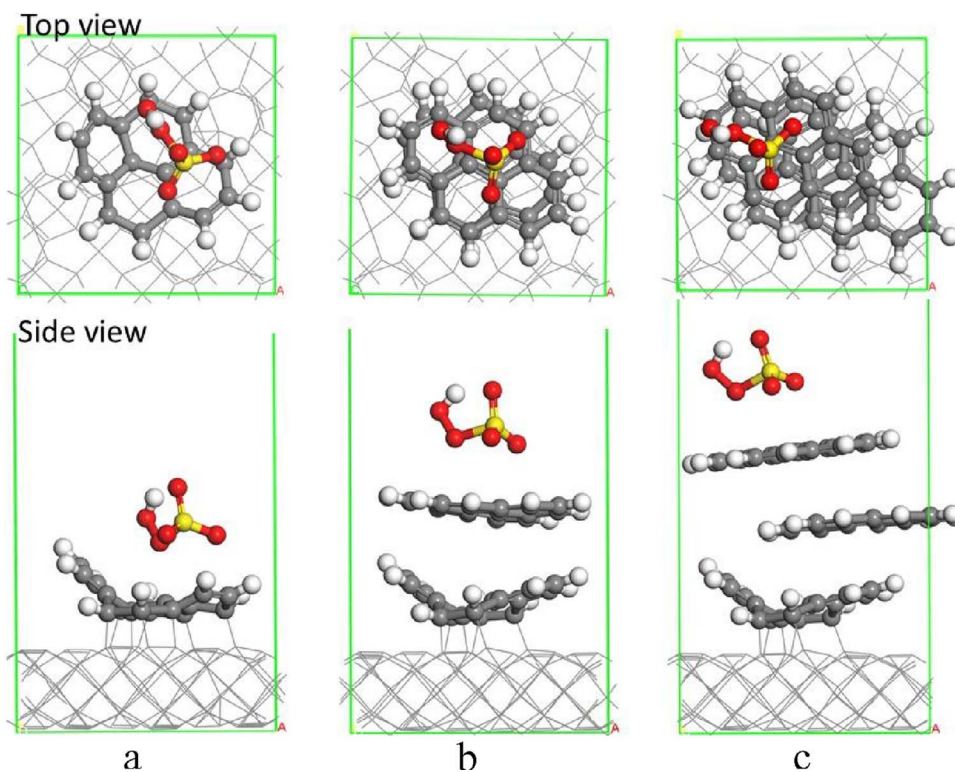


Fig. 3. The relaxed configuration of PMS adsorption on graphene/diamond system with different layers of graphene. (a) 1 layer graphene, (b) 2 layers graphene, (c) 3 layers graphene.

categories and contents of sp^2/sp^3 carbons as well as defective/graphitic degree, not applied in this study though.

3.2. Theoretical evaluation of PMS adsorption on the sp^2/sp^3 hybrid structure

We utilized theoretical calculations to simulate the PMS molecular adsorption onto the annealed nanodiamonds with different graphitization degrees. The graphene/diamonds with 1–3 graphene layers were built and the corresponding relaxed structures are presented in Fig. 3. The top graphene layer was discovered to present a strong covalent bonding with the diamond surface. When the second and third graphene flakes were constructed above, the graphene lattices would intimately interact with each other via the van der Waals attractions. In regard to the adsorption behavior of PMS, the oxidant molecule (PMS) exhibited a preferable tendency to lie down onto the outer graphene via chemical bonding with the graphene surface regardless the thickness of the shells. To better illustrate the interaction of PMS with the graphene/diamond composites and the activation of PMS in the different scenarios of variable graphene layers, several key parameters, such as bond length (l_{O-O}) of SO_3O-OH (PMS molecule), charge transfer (Q) from the substrate to PMS, adsorption energy (E_{ads}) and total net charge population (Q_{C-net}) of the carbon atoms in the outer graphene lattice are listed in Table 1.

The effective activation of PMS molecules is dependent on breaking up the peroxide O–O bond and achieving charge-transport from catalysts. Thus, the bond length and charge density of PMS will predict the

activation process when interacting with the catalyst surface. In this study, the cleavage of PMS and charge-transport number exhibited different trends with the increased graphene layers. Compared with the natural PMS with a SO_3O-OH bond length at 1.326 Å, the l_{O-O} was stretched significantly to 1.421 Å for the one-layer graphene/diamond, and 1.410 Å for the two/three-layer models, which implies the activation of the PMS molecule on the hybrid surface. The electron-transfer from outer graphene of the hybrid to PMS was 0.553 e, 0.455 e, and 0.454 e for one, two, and three layer-graphene models, respectively. Increasing the graphene layer number from one to two leads to lower charge-transport from graphene to PMS, less electron-density (Fig. S7 and Table S3), and a shorter bond length of superoxide O–O bond. A further increase of the layers to three shows a marginal effect. The theoretical prediction is in good agreement with the experiment that S-ND-1100 with multi-graphitic shells is less reactive than S-ND-900 with a single shell for PMS activation and catalytic oxidation.

We further employed carbon nanotubes (CNT) with different wall thicknesses for PMS activation as shown in Fig. S8 and Table S4. Similarly, the single-walled CNT exhibited the best catalytic activity for organic oxidation with a rate constant of 0.020 min^{-1} , which decreased to 0.008 and 0.006 min^{-1} on double-walled and multi-walled (> 12 layers) CNTs, suggesting that the multi-graphitic layers interacted via the van der Waals forces might limit the synergistic effect for PMS activation. However, the superb catalytic efficiency of single-layer graphene/diamond was benefited from the hybrid structure that the inner diamond substrate can effectively excite electrons to the conjugated π system of nearby graphene via the covalent bonds, giving rise to a denser electron population for transferring electrons to PMS molecule [26]. This is verified by the net charge density (Table 1) of outer graphene lattice (Q_{C-net}) which for a single layer (−0.746 e) is more negative than that for the two (−0.549 e) or three (−0.486 e) layers. We speculate that the tunnelling effect might be weakened because very few electrons could penetrate the graphene/diamond (covalent bond) and graphene/graphene (van der Waals interaction) interfaces to reach the outermost shell in a multi-layered structure. It should be pointed out that we engaged a graphene lattice here instead of a fullerene structure to simplify the model for calculation. In reality, the charge

Table 1

The relevant calculation results of PMS adsorption on diamond/multi-layer graphene. (The l_{O-O} in free PMS is 1.326 Å).

Configuration	l_{O-O} (Å)	$Q(e)$	Q_{C-net}	E_{ads} (eV)
1 layer graphene/diamond	1.421	−0.553	−0.746	−2.46
2 layer graphene/diamond	1.410	−0.455	−0.549	−2.939
3-layer graphene/diamond	1.410	−0.454	−0.486	−3.157

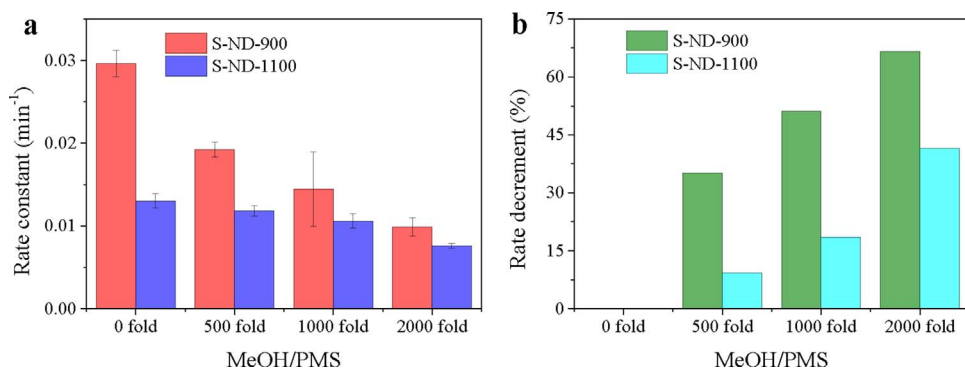


Fig. 4. Radical quenching effects on (a) reaction rate of phenol oxidation and (b) rate decrement percentage with different loadings of methanol in S-ND-900/PMS and S-ND-1100/PMS.

distribution is uneven for the concave and convex sides of graphitic sphere of annealed nanodiamonds, because the carbon atoms in the curvature structure (similar to carbon nanotubes) could excite electrons to the π orbitals of the bent outer shell, thereby resulting in a denser electron population of the delocalized π system [1,27,28]. Herein, the electron-enriched convexity of the fullerene shell may further enhance the catalytic performance of the hybrid for PMS activation.

Nevertheless, one-layer graphene/nanodiamond induces longer $l_{\text{O-O}}$ and greater Q for PMS activation, and the model shows the highest adsorption energy (E_{ads}) of -2.460 eV in contrast to two- and three-layer graphene of -2.939 and -3.157 eV accordingly. A moderate adsorption energy may facilitate the detachment of the cleaved PMS molecules to produce hydroxyl and/or sulfate radicals. Since both hydroxyl and sulfate radicals could be generated in PMS activation, the competitive radical quenching test was performed (Fig. S9), which indicates that sulfate radicals are the dominating oxidative species among the free radicals in S-ND-900/PMS. This is further supported by Fig. S10 that the system is less effective for oxidation of nitrobenzene and benzoic acid, typical hydroxyl radical probes. Interestingly, introducing excessive methanol (the radical scavenger, $k_{\text{SO}_4\cdot^-} = 3.2 \times 10^6$, $k_{\cdot\text{OH}} = 9.7 \times 10^8$) at 1000-times of PMS did not completely terminate the oxidation reaction and 87.8% phenol oxidation was still achieved in 120 min. This is intrinsically different from the classical $\text{SO}_4\cdot^-$ -dominated system of Co^{2+} /PMS, and $\cdot\text{OH}$ -based system of $\text{Fe}^{2+}/\text{H}_2\text{O}_2$ where the oxidations could be instantly ceased (Fig. S11).

3.3. Transition from radical to nonradical pathway on annealed nanodiamond

In previous studies, we unveiled that PMS activation by carbocatalysis involved both radical and nonradical oxidations, whereas the mechanism of the nonradical process remains ambiguous and that rational governing the pathways is difficult to achieve [29,30]. It was supposed that, in a nonradical process, the PMS molecules were activated on the surface of carbocatalysts to form a reactive intermediate or surface-bonded sulfate radical, which directly reacts with the organic contaminants via a rapid electron transfer without generation of free radicals into the aqueous phase [31–33]. Since the activated complexes are confined on the surface, the reactive intermediates usually presented a mild redox potential, leading to a good selectivity to electron-rich substances [33–36].

For the graphene/diamond hybrids, DFT calculations indicate that PMS adsorption onto the composites with 2–3 graphene layers becomes stronger (lower E_{ads}), yet exhibits a shorter bond length of $\text{HO-O}(\text{SO}_3)$ and less electron transfer from the graphene (Table 1). This interesting finding suggested that multi-graphitic layers promote the interaction with PMS molecules, yet are not beneficial for O–O bond cleaving to produce free radicals, which might foresee a different activation pathway on the nanodiamonds. PMS may be intimately attached onto the carbon surface (without producing radicals to the solution) to form a reactive intermediate towards phenol oxidation, namely a nonradical

process. To verify the hypothesis, we compared the oxidative performances of S-ND-900 and S-ND-1100 under different dosages of methanol in solutions (Figs. S12 and S13). It is interesting to find in Fig. 4a that the S-ND-900 is more sensitive to radical scavengers than S-ND-1100 and the reaction rate decreased rapidly with the increased loading of methanol. Moreover, Fig. 4b manifests that the organic oxidation rates of S-ND-900 were declined by 35.0, 48.9, and 66.6% with the addition of methanol at 500-, 1000-, and 2000-fold, respectively, compared with the control experiment without any alcohol, whereas S-ND-1100 exhibited much better resistance to the radical scavenger with a decline rate of 9.2, 18.5, and 41.5% accordingly. The S-ND-1100 obviously exhibited a better resistance to the radical scavenger than S-ND-900. Given the fact that a typical $\text{SO}_4\cdot^-/\cdot\text{OH}$ -based system could be immediately terminated by excessive methanol (1000-fold of the oxidant) in Fig. S11, the contributions of phenol oxidation by the nonradical pathway in S-ND-900/PMS and S-ND-1100/PMS were estimated to be 33.4% and 58.5%, respectively. Therefore, the radical quenching tests suggest that the higher graphitic degree on S-ND-1100 gives rise to a greater proportion of nonradical oxidation and the formation of multi-graphitic layers facilitate the transformation of radical-based pathway to a nonradical process for catalytic oxidation, which is good consistence with the theoretical prediction.

4. Conclusions

Surface-modified nanodiamonds by thermal annealing have been demonstrated as a carbon sp^2/sp^3 structured model in a chemical reaction of peroxymonosulfate activation and catalytic oxidation for mechanistic insights into the structure-activity from the viewpoints of theoretical calculation and experiment. The superb catalytic activity of annealed nanodiamonds is originated from a synergistic effect of the self-constructed sp^2/sp^3 hybrid structure that enriched the charge density of graphitic carbon surface and promoted the electron-transfer to PMS molecules. More importantly, theoretical calculation and experimental design unveiled that the activation pathway of peroxymonosulfate was sensitive to the thickness of the graphitic shell on the diamond, and further increasing the wall number would transfer the radical-dominated oxidation to a nonradical-based pathway. Due to the moderate redox potential of a nonradical process in which the PMS was partially confined on the carbon surface, the nanodiamond/PMS would be able to provide a tuneable and mild oxidative potential for selective oxidation of organic compounds in complicated water matrix. Hence, the manipulated nonradical oxidation with carbocatalysis may provide a promising oxidative system for organic synthesis (e.g. selective oxidation) and hydrocarbon conversions in aqueous and nonaqueous phases.

Acknowledgements

The authors acknowledge the ARC Discovery Projects (DP150103026 and DP170104264). ZA would like to thank the “1000

plan” for Young Professionals Program of China, “100 Talents” Program of Guangdong University of Technology, and National Natural Science Foundation of China (Grant No. 21607029). XD thanks Prof. Sanping Jiang and Dr. Yi Cheng at Curtin University for fruitful discussions and providing the carbon nanotubes.

Appendix A. Supplementary data

Supplementary data associated with this article can be found, in the online version, at <http://dx.doi.org/10.1016/j.apcatb.2017.10.007>.

References

- [1] X.K. Kong, C.L. Chen, Q.W. Chen, *Chem. Soc. Rev.* 43 (2014) 2841–2857.
- [2] D.S. Geng, Y. Chen, Y.G. Chen, Y.L. Li, R.Y. Li, X.L. Sun, S.Y. Ye, S. Knights, *Environ. Sci.* 4 (2011) 760–764.
- [3] S. Navalón, A. Dhakshinamoorthy, M. Alvaro, M. Antonietti, H. Garcia, *Chem. Soc. Rev.* 46 (2017) 4501–4529.
- [4] S. Navalón, A. Dhakshinamoorthy, M. Alvaro, H. Garcia, *Chem. Rev.* 114 (2014) 6179–6212.
- [5] K.P. Gong, F. Du, Z.H. Xia, M. Durstock, L.M. Dai, *Science* 323 (2009) 760–764.
- [6] J. Zhang, X. Liu, R. Blume, A.H. Zhang, R. Schlögl, D.S. Su, *Science* 322 (2008) 73–77.
- [7] Y.G. Li, W. Zhou, H.L. Wang, L.M. Xie, Y.Y. Liang, F. Wei, J.C. Idrobo, S.J. Pennycook, H.J. Dai, *Nat. Nanotechnol.* 7 (2012) 394–400.
- [8] Z.J. Fan, J. Yan, L.J. Zhi, Q. Zhang, T. Wei, J. Feng, M.L. Zhang, W.Z. Qian, F. Wei, *Adv. Mater.* 22 (2010) 3723–3728.
- [9] V.C. Tung, L.M. Chen, M.J. Allen, J.K. Wassei, K. Nelson, R.B. Kaner, Y. Yang, *Nano Lett.* 9 (2009) 1949–1955.
- [10] S. Osswald, G. Yushin, V. Mochalin, S.O. Kucheyev, Y. Gogotsi, *J. Am. Chem. Soc.* 128 (2006) 11635–11642.
- [11] A. Krueger, *J. Mater. Chem.* 18 (2008) 1485–1492.
- [12] M. Zeiger, N. Jackel, M. Asian, D. Weingarth, V. Presser, *Carbon* 84 (2015) 584–598.
- [13] X.G. Duan, C. Su, L. Zhou, H.Q. Sun, A. Suvorova, T. Odedairo, Z.H. Zhu, Z.P. Shao, S.B. Wang, *Appl. Catal. B* 194 (2016) 7–15.
- [14] X. Liu, B. Frank, W. Zhang, T.P. Cotter, R. Schlögl, D.S. Su, *Angew. Chem. Int. Ed.* 50 (2011) 3318–3322.
- [15] Y.S. Zhu, Y.M. Lin, B.S. Zhang, J.F. Rong, B.N. Zong, D.S. Su, *Chemcatchem* 7 (2015) 2840–2845.
- [16] T. Petit, J.C. Arnault, H.A. Girard, M. Sennour, P. Bergonzo, *Phys. Rev. B* 84 (2011) 233407.
- [17] J.A. Zhang, D.S. Su, R. Blume, R. Schlögl, R. Wang, X.G. Yang, A. Gajovic, *Angew. Chem. Int. Ed.* 49 (2010) 8640–8644.
- [18] Y.M. Lin, D.S. Su, *ACS Nano* 8 (2014) 7823–7833.
- [19] V.L. Kuznetsov, A.L. Chuvilin, Y.V. Butenko, S.V. Stankus, R.A. Khairulin, A.K. Gutakovskii, *Chem. Phys. Lett.* 289 (1998) 353–360.
- [20] Y.M. Chi, M.L. Zhu, Y.H. Li, H. Yu, H.J. Wang, F. Peng, *Catal. Sci. Technol.* 6 (2016) 2396–2402.
- [21] J.C. Espinosa, S. Navalón, A. Primo, M. Moral, J.F. Sanz, M. Alvaro, H. Garcia, *Chem. Eur. J.* 21 (2015) 11966–11971.
- [22] Y.M. Lin, X.L. Pan, W. Qi, B.S. Zhang, D.S. Su, *J. Mater. Chem. A* 2 (2014) 12475–12483.
- [23] S. Turner, O.I. Lebedev, O. Shenderova, I.I. Vlasov, J. Verbeeck, G. Van Tendeloo, *Adv. Funct. Mater.* 19 (2009) 2116–2124.
- [24] A.A. Soltamova, I.V. Ilyin, P.G. Baranov, A.Y. Vul', S.V. Kidalov, F.M. Shakhov, G.V. Mamin, S.B. Orlinskii, N.I. Silkin, M.K. Salakhov, *Physica. B* 404 (2009) 4518–4521.
- [25] E. Colineau, A. Deneuville, J. Mambou, E. Gheeraert, *Appl. Phys. Lett.* 68 (1996) 2123–2125.
- [26] X.G. Duan, Z.M. Ao, D.G. Li, H.Q. Sun, L. Zhou, A. Suvorova, M. Saunders, G.X. Wang, S.B. Wang, *Carbon* 103 (2016) 404–411.
- [27] D.S. Su, G. Wen, S. Wu, F. Peng, R. Schlögl, *Angew. Chem. Int. Ed.* (2016) 936–964.
- [28] J.M. Carlsson, M. Scheffler, *Phys. Rev. Lett.* 96 (2006) 046806.
- [29] X.G. Duan, H.Q. Sun, Y.X. Wang, J. Kang, S.B. Wang, *ACS Catal.* 5 (2015) 553–559.
- [30] X.G. Duan, Z.M. Ao, L. Zhou, H.Q. Sun, G.X. Wang, S.B. Wang, *Appl. Catal. B* 188 (2016) 98–105.
- [31] T. Zhang, Y. Chen, Y. Wang, J. Le Roux, Y. Yang, J.-P. Croué, *Environ. Sci. Technol.* 48 (2014) 5868–5875.
- [32] H. Lee, H.J. Lee, J. Jeong, J. Lee, N.B. Park, C. Lee, *Chem. Eng. J.* 266 (2015) 28–33.
- [33] X.B. Wang, Y.L. Qin, L.H. Zhu, H.Q. Tang, *Environ. Sci. Technol.* 49 (2015) 6855–6864.
- [34] H. Lee, H.I. Kim, S. Weon, W. Choi, Y.S. Hwang, J. Seo, C. Lee, J.H. Kim, *Environ. Sci. Technol.* 50 (2016) 10134–10142.
- [35] H. Song, L. Yan, J. Ma, J. Jiang, G. Cai, W. Zhang, Z. Zhang, J. Zhang, T. Yang, *Water Res.* 116 (2017) 182–193.
- [36] D. Li, X. Duan, H. Sun, J. Kang, H. Zhang, M.O. Tade, S. Wang, *Carbon* 115 (2017) 649–658.